

Three-Dimensional Modelling of the Dynamics of Therapeutic Ultrasound Contrast Agents

Chao-Tsung Hsiao* / DYNAFLOW, INC

Xiaozhen Lu / DYNAFLOW, INC

Georges L. Chahine / DYNAFLOW, INC

ctsung@dynaflo-inc.com

ABSTRACT

A 3-D thick-shell contrast agent dynamics model was developed by coupling a finite volume Navier-Stokes solver, DF-UNCLE[®], and a potential Boundary Element Method flow solver, 3DYNAFS[®], to simulate the dynamics of thick-shelled contrast agents subjected to pressure waves. The 3-D model was validated using a spherical thick shell model validated by experimental observations. We then utilized this model to study shell break-up during non-spherical deformations resulting from multiple contrast agent interaction or the presence of a nearby solid wall. Our simulations indicate that the thick viscous shell prevents the contrast agent from forming a reentrant jet, as normally observed for an air bubble oscillating near a solid wall. Instead, the shell thickness varies significantly from location to location during the dynamics and this could lead to break up due to local shell thinning and stretching.

1. INTRODUCTION

Ultrasound contrast agents are encapsulated microbubbles usually formed of a high molecular weight gas core and a viscous shell [1]. A wide variety of materials have been used for the shell material such as oils, lipids, rigid polymers, and albumins. Ultrasound contrast agents, originally developed to enhance diagnostic imaging, have recently been incorporated into therapeutic applications. The capability of delivering drug to the targeted area makes therapeutic ultrasound contrast agents attractive to chemotherapy drug development because many chemotherapy drugs are toxic to normal tissues. For therapeutic ultrasound contrast agents, the drug is suspended within a highly viscous thick liquid shell [2]. The highly viscous shell stabilizes the encapsulated bubble and remains inert until the contrast agent reaches a specific target. The encapsulated microbubble is then excited with an appropriate acoustic amplitude and frequency, to get it to break up and release the drugs. A right selection of shell material and thickness and an appropriate use of ultrasound renders the contrast agents powerful targeted drug delivery vehicles.

Characterization and understanding of the fragmentation mechanism of a contrast agent is pivotal to its use for drug delivery. The ultrasonic fragmentation threshold depends on the initial size, shell thickness, and shell and gas properties [3,4]. Using a high intensity source and a large number of cycles may

be applicable to all types and sizes of contrast agent, but cannot be applied safely in a clinical environment. Understanding of the forces involved in the breakup of a particular type of agent is therefore paramount to avoiding expensive and lengthy trial and error experiments, and to minimizing risk to patients. Presently, however, the dynamic mechanisms involved in shell breakup are not well understood. These mechanisms become even more complicated when the contrast agent 'bubble' interacts with other agents and/or nearby tissues. From previous studies on bubble dynamics [5-7], it is known that an oscillating bubble near a boundary may form a re-entrant jet during its non-spherical collapse depending on its distance to nearby bubbles and boundaries. A similar behaviour is expected with the ultrasound contrast agents. Indeed, micro-jetting and micro-streaming associated with the agent violent non-spherical breakup have been hypothesized as mechanisms to enhance drug delivery [8].

Many studies have been dedicated to developing numerical models for ultrasound contrast agents. Many models stem from Church's pioneering work [9]. With a thin-shell assumption the constitutive equation of the shell was simplified and incorporated into a generalized Rayleigh-Plesset formulation with a balance of the radial stress at the solid-liquid interface. The resulting model has been adapted to study the effect the encapsulating shell properties on the microbubble dynamics [10,11] and to estimate the acoustic nonlinearity of the liquid containing encapsulated microbubbles [12]. More recently, Sarkar *et al.* [13] proposed a further refined model. The assumption of a thin solid shell is reasonable for contrast agents designed for imaging purpose, with a very thin lipid or protein shell on the order of a few nanometres. However, prototype therapeutic contrast agents are designed with a thick liquid shell to enable drug transport [2]. Allen *et al.* [14] extended Church's model to take into account the thick liquid shell and compared their results with experimental measurements [15]. Their study was however limited to spherical agents and no deformations were included such as what results from the interaction between the agent and its surroundings, or what happens at bursting under a strong acoustic field.

To investigate the detailed dynamic mechanisms which cause shell breakup, we have developed in the work presented here a 3-D non-spherical finite-thickness shell model which

couples a Navier-Stokes solver, DF-UNCLE[®], derived from UNCLE originally developed by Mississippi State University, using a finite volume scheme and our potential flow solver, 3DYNAPS[®], using a Boundary Element Method (BEM). The computational domain was subdivided into an inner domain constituted of the thick viscous shell layer and an outer domain; that of the liquid containing the shelled bubble. In the inner domain we solve the Navier-Stokes equations to best describe the dynamical behavior of the highly viscous liquid shell. In the outer domain we use the Boundary Element Method. The main advantage of using the BEM is its unique ability to provide a complete solution in terms of boundary values without need to discretize the whole computational domain. This reduces the dimensions of the problem by one. This allows the model to work on complicated boundary geometries and addresses non-spherical deformations.

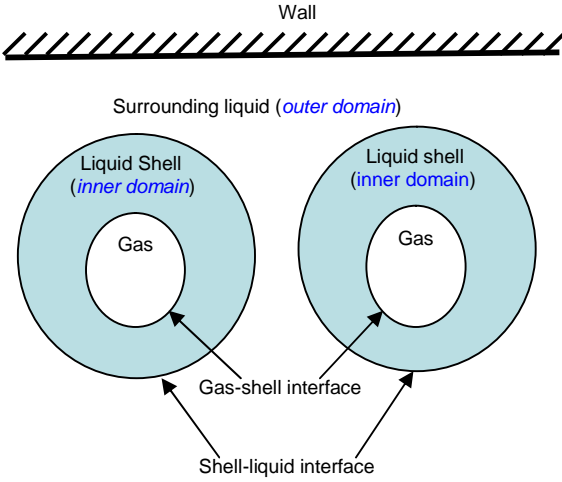


Figure 1. Sketch for illustration of the thick shell bubble problem with domain decomposition.

2. NUMERICAL MODELS

2.1. Domain Decomposition

Consider a problem in which multiple ultrasound contrast agent shelled bubbles interact with each other and with nearby boundaries. The computational domain for this problem, as illustrated in Figure 1, is composed of as many *inner domains* as bubbles made each of a thick liquid shell around each gas bubble and an *outer domain* covering the host liquid medium. The outer domain includes any nearby walls or free surfaces. In the model developed here, the inner domains bounded by the gas-shell interfaces and the shell-liquid interface are volume discretized. The flow field within the shell layer is solved using the unsteady Navier-Stokes equations, while the flow field in the outer domain, which is much less viscous, is solved assuming a potential flow. The two solvers communicate with each other by exchanging the values of the flow variables at the shell-liquid interfaces.

2.2. Model for the Shell Liquid: Inner Domain

2.2.1. Governing Equation

To solve the highly viscous flow in the *inner domain* composed of the viscous shells, the unsteady incompressible

Navier-Stokes equations are used. The continuity and momentum equations in non-dimensional form and Cartesian tensor notations are given as:

$$\frac{\partial u_i}{\partial x_i} = 0, \quad (1)$$

$$\frac{\partial u_i}{\partial t} + u_j \frac{\partial u_i}{\partial x_j} = -\frac{\partial p}{\partial x_i} + \frac{1}{R_e} \frac{\partial \tau_{ij}}{\partial x_j}, \quad (2)$$

where $u_i = (u, v, w)$ are the Cartesian components of the velocity, $x_i = (x, y, z)$ are the Cartesian coordinates, and p is the pressure. $R_e = \rho_s u^* L^* / \mu_s$ is the Reynolds number of the viscous shell, u^* and L^* are the characteristic velocity and length, ρ_s is the shell density, and μ_s is its dynamic viscosity.

We select as characteristic length the contrast agent initial inner radius. The characteristic velocity, $u^* = L^* / T^*$, can be selected by two ways depending on the characteristic time, T^* , which could be the inverse of the frequency of the imposed acoustic waves or could be based on Δp the amplitude of the imposed acoustic waves,

$$T^* = L^* \sqrt{\frac{\rho_s}{\Delta p}}. \quad (3)$$

In our computations T^* was selected to be the smaller of the two choices.

The effective stress tensor τ_{ij} is given by:

$$\tau_{ij} = \left[\left(\frac{\partial u_i}{\partial x_j} + \frac{\partial u_j}{\partial x_i} \right) - \frac{2}{3} \delta_{ij} \frac{\partial u_k}{\partial x_k} \right], \quad (4)$$

where δ_{ij} is the Kronecker delta. The flow field in the *inner domain* is directly simulated with Equations (1) and (2) without any turbulence model because the Reynolds number is very small and the flow is laminar for all cases studied.

In order to simplify the treatment of the boundary conditions for complex geometries, Equations (1) and (2) are expressed into a general time-dependent body-fitted curvilinear coordinate system. The time dependent nature of this transformation allows all computations to be carried out in a fixed uniform computational domain even though components of the physical domain may be in motion. The curvilinear coordinates are defined as:

$$\begin{aligned} \tau &= t, \\ \xi &= \xi(x, y, z, t), \\ \eta &= \eta(x, y, z, t), \\ \zeta &= \zeta(x, y, z, t). \end{aligned} \quad (5)$$

The transformation provides a computational domain that is better for applying spatial differencing and the boundary conditions.

2.2.2. Boundary condition at the gas-shell interface

The gas-shell interface is treated as a standard gas-liquid interface, which can be best described by a free surface boundary condition satisfying both kinematic and dynamic boundary conditions. The kinematic condition is that a particle

on the surface remains on the surface. For a surface of equation $F(x_i, t) = 0$, this can be written $DF/Dt = 0$.

The dynamic condition imposes zero shear stress (we ignore here stress generated by the air in the bubble) and balance of normal stresses at the interface. With the same simplifications used by Batchelor [16] for deriving the dynamic boundary condition in the Cartesian coordinate system, Hodges et al. [17] derived a dynamic boundary condition in a curvilinear coordinate system by requiring the grid to be normal to the boundary. Following their work we write the dynamic boundary condition at $\zeta=0$ (gas-shell interface) in non-dimensional form as:

$$\left. \frac{\partial U}{\partial \zeta} \right|_{\zeta=0} = 0, \quad (6)$$

$$\left. \frac{\partial V}{\partial \zeta} \right|_{\zeta=0} = 0, \quad (7)$$

$$p = p_{gv} + \frac{2}{R_e} \left. \frac{\partial W}{\partial \zeta} \right|_{\zeta=0} - \frac{\mathcal{C}_{gs}}{W_{e,gs}}, \quad (8)$$

where (U, V, W) are contravariant velocity components in the curvilinear coordinates and \mathcal{C}_{gs} is the curvature of gas-shell interface.

$$W_{e,gs} = \rho_s u^{*2} L^* / \gamma_{gs}, \quad (9)$$

is the Weber number with γ_{gs} being the surface tension at the gas-shell interface.

$$p_{gv} = (p_g + p_v - p_\infty) / \rho_s u^{*2}. \quad (10)$$

To determine the gas pressure we assume that the amount of gas inside the bubble remains constant and that the gas satisfies the polytropic relation:

$$p_g \mathcal{V}^k = \text{constant}, \quad (11)$$

where \mathcal{V} is the gas volume.

2.2.3. Boundary condition at the shell-liquid interface

The shell-liquid interface is a liquid-liquid interface at which the boundary conditions are continuity of the shear stresses, balance of the normal stresses, and continuity of the velocity:

$$\left. \frac{\partial U}{\partial \zeta} \right|_{\zeta=1} = \frac{\mu_l}{\mu_s} \tau_{l,\xi}, \quad (12)$$

$$\left. \frac{\partial V}{\partial \zeta} \right|_{\zeta=1} = \frac{\mu_l}{\mu_s} \tau_{l,\eta}, \quad (13)$$

$$p - \frac{2}{R_e} \left. \frac{\partial W}{\partial \zeta} \right|_{\zeta=1} = P_l - \frac{1}{R_e} \frac{\mu_l}{\mu_s} \tau_{l,\zeta} + \frac{\mathcal{C}_{sl}}{W_{e,sl}}, \quad (14)$$

$$W|_{\zeta=1} = \mathbf{u}_s \cdot \mathbf{n}, \quad (15)$$

where μ_l is the dynamic viscosity of the surrounding liquid, ρ_l is its density, \mathcal{C}_{sl} is the curvature of the shell-liquid interface.

$$W_{e,sl} = \rho_s u^{*2} L^* / \gamma_{sl}, \quad (16)$$

is the Weber number, where γ_{sl} is the surface tension at the shell-liquid interface.

$\tau_{l,\xi}$, $\tau_{l,\eta}$ are the normal derivatives of the tangential velocity components in the ξ and η directions respectively at the liquid side of the interface. $\tau_{l,\zeta}$ is the normal derivative of the normal velocity component, and P_l is the pressure on the liquid side of the shell-liquid. \mathbf{n} is the local unit normal vector to the boundary and \mathbf{u}_s is the viscous liquid velocity at the boundary which will be provided by the solution of the outer domain,

In this study we further simplified the boundary condition and consider cases where viscosity of the shell material used for therapeutic ultrasound contrast agents is much higher than the viscosity of the surrounding liquid. This is usually the case in order to stabilize the contrast agent during transit. For example, ImaRx Therapeutics (Tucson, AZ) has produced two types of prototype agents with a triacetin shell and a soybean oil shell. The viscosities of triacetin and soybean oil are 28 centipoise and 110 centipoise respectively which are much larger (at least one order larger) than the viscosity of blood (2.7 centipoise at 37°C). If the viscosity ratio μ_l/μ_s are very small, Equations (12)-(14) can be reduced to:

$$\left. \frac{\partial U}{\partial \zeta} \right|_{\zeta=1} = 0, \quad (17)$$

$$\left. \frac{\partial V}{\partial \zeta} \right|_{\zeta=1} = 0, \quad (18)$$

$$p - \frac{2}{R_e} \left. \frac{\partial W}{\partial \zeta} \right|_{\zeta=1} = P_l + \frac{\mathcal{C}_{sl}}{W_{e,sl}}. \quad (19)$$

2.2.4. Numerical Approach

The DF-UNCLE[®] code is based on the artificial-compressibility method [18] in which a time derivative of the pressure is added to the continuity equation as

$$\frac{1}{\beta} \frac{\partial p}{\partial t} + \frac{\partial u_i}{\partial x_i} = 0, \quad (20)$$

where β is an artificial compressibility factor. As a consequence, the hyperbolic system of equations formed can be solved using a time marching scheme.

The solution procedure is to march in pseudo-time until reaching a steady-state solution. To obtain a time-dependent solution, a Newton iterative procedure is performed at each physical time step in order to satisfy the continuity equations. The numerical scheme in DF-UNCLE[®] uses a finite volume formulation. The first-order Euler implicit difference formula is applied to the time derivatives. The spatial differencing of the convective terms uses the flux-difference splitting scheme based on Roe's method [19] and van Leer's MUSCL method [20] for obtaining the first-order and the third-order fluxes respectively. A second-order central differencing is used for the viscous terms. The flux Jacobians required in an implicit scheme are obtained numerically. The resulting system of algebraic equations is solved using the Discretized Newton Relaxation method [21] in which symmetric block Gauss-Seidel sub-iterations are performed before the solution is updated at each Newton interaction.

2.3. Model for Surrounding Liquid: Outer Domain

2.3.1. Governing Equations

The outer domain liquid flow due to the contrast agent's motion is assumed to be irrotational and incompressible. These are conventional assumptions for bubble dynamics [22,23] The assumption of irrotational flow for the outer domain allows the definition of a velocity potential, ϕ , such that

$$\mathbf{u} = \nabla \phi, \quad (21)$$

where \mathbf{u} is the velocity vector. The assumption that the liquid is incompressible leads to Laplace's equation for the potential:

$$\nabla^2 \phi = 0. \quad (22)$$

A boundary integral method is used to solve Equation (16). This method is based on an integral solution of the Laplace equation using Green's theorem, which can be written in the following form:

$$\int_{\Omega} (\phi \nabla^2 G - G \nabla^2 \phi) d\Omega = \int_S \mathbf{n} \cdot [\phi \nabla G - G \nabla \phi] dS. \quad (23)$$

In this expression Ω is the domain of integration having elementary volume $d\Omega$. The boundary surface of Ω is S which includes the surface of the contrast agent and the nearby boundaries with elementary surface element dS and local normal unit vector \mathbf{n} . ϕ is harmonic in the fluid domain Ω , and G is Green's function. If G is selected to be harmonic everywhere but at some discrete points, Equation (17) simplifies considerably. For instance, if

$$G = -\frac{1}{|\mathbf{x} - \mathbf{y}|}, \quad (24)$$

where \mathbf{x} is a fixed point in Ω and \mathbf{y} is a point on the boundary surface S , Equation (21) reduces to Green's formula with $\alpha\pi$ being the solid angle at \mathbf{x} enclosing the domain Ω :

$$\alpha\pi\phi(\mathbf{x}) = \int_S \mathbf{n}_y \cdot [\phi(\mathbf{y})\nabla G(\mathbf{x},\mathbf{y}) - G(\mathbf{x},\mathbf{y})\nabla\phi(\mathbf{y})] dS, \quad (25)$$

- $\alpha = 4$, if \mathbf{x} is a point in the fluid,
- $\alpha = 2$, if \mathbf{x} is a point on a smooth surface, and
- $\alpha < 4$, if \mathbf{x} is a point at a sharp corner of the discretized surface.

This equation states that if the velocity potential ϕ and its normal derivatives are known on the boundary surface S of a domain Ω , where ϕ satisfies the Laplace equation, then ϕ can be determined anywhere in Ω by integration over the boundary surface. Using this expression the boundary integral method reduces by one the dimension of the problem of solving the Laplace equation.

2.3.2. Boundary Conditions

At any given time step, if the velocity potential ϕ on the boundary surface S is known, then the interface normal velocity $\partial\phi/\partial n$ can be obtained by Equation(25). For a point \mathbf{x} on the boundary S , the Bernoulli equation gives

$$P_i + \rho_l \left[\frac{\partial\phi}{\partial t} + \frac{1}{2} \nabla\phi \cdot \nabla\phi \right] = P(t), \quad (26)$$

where $P(t)$ is the acoustic pressure imposed and the pressure on the interface P_i is obtained by Equation (19). Equation (26)

provides $\partial\phi/\partial t$, and the rate of change in potential at a given point followed in its motion can be obtained by

$$\frac{D\phi}{Dt} = \frac{\partial\phi}{\partial t} + \mathbf{u}_s \cdot \nabla\phi, \quad (27)$$

where \mathbf{u}_s is the shell velocity at the shell-liquid interface as defined in Equation (15). Since no liquid is allowed to cross the shell-liquid interface, the normal velocity component of the shell velocity at the interface must be equal to the normal velocity component of the liquid, i.e.

$$\mathbf{u}_s \cdot \mathbf{n} = \frac{\partial\phi}{\partial n}. \quad (28)$$

2.3.3. Numerical Approach

To solve Equation (25) numerically with the boundary element method, it is necessary to discretize the surfaces of all objects. As a result of this discretization, every surface integral evaluated at any field point \mathbf{x} becomes a summation over all panels of the influence of singularity distributions over each individual panel. This enables us to write Green's identity in the form

$$\alpha\pi\phi(\mathbf{x}) = \sum_{k=1}^P \int_{S_k} \left(\phi(\mathbf{y}) \frac{\partial G}{\partial n}(\mathbf{x},\mathbf{y}) - G(\mathbf{x},\mathbf{y}) \frac{\partial\phi}{\partial n}(\mathbf{y}) \right) dS_k, \quad (29)$$

where P is the number of surface elements on the boundary. To evaluate the integrals given in Equation (29), it is necessary to assume a relation between ϕ and $\partial\phi/\partial n$ at a surface node with the values of these quantities at the discretized nodes. Here, we assume that these quantities vary linearly over a panel and can be described by the surrounding nodes. By applying a linear interpolation for each panel S_k , each elementary integral can be written as a linear combination of ϕ or $\partial\phi/\partial n$ evaluated at the surrounding nodes. The integration expressions are complex, and details can be found in our previous studies [24]. With the integration over each panel performed, the discretized Equation (29) can be expressed as:

$$\alpha\pi\phi_j = \sum_{k=1}^P \sum_{i=1}^m \left[B_i^k \phi_i^k - A_i^k \left(\frac{\partial\phi}{\partial n} \right)_i^k \right], \quad (30)$$

$$j = 1, N, \quad m = \begin{cases} 3 & \text{triangular element,} \\ 4 & \text{quadrilateral element,} \end{cases}$$

where ϕ_i^k and $\partial\phi/\partial n_i^k$ are the potential and its normal derivative at node i of panel k , and A_i^k and B_i^k are influence coefficients obtained from elementary integration and N is the total node number.

Following a "collection" approach in which the contributions due to the same node are collected from the various contiguous elementary surfaces and summed up, Equation (30) can be rewritten as:

$$\alpha\pi\phi_j = \sum_{i=1}^N \left[\bar{B}_i \phi_i - \bar{A}_i \left(\frac{\partial\phi}{\partial n} \right)_i \right], \quad j = 1, N, \quad (31)$$

where \bar{A} and \bar{B} are the altered influence coefficients due to summation of the same node. It is noted that the "collection" approach transfers the panel contribution in Equation (30) to the node contribution in Equation (31). Equation (31) can be expressed in a matrix form as:

$$\bar{\mathbf{B}} \frac{\partial \phi}{\partial n} = (a\pi \mathbf{I} + \bar{\mathbf{A}}) \phi, \quad (32)$$

where \mathbf{I} is an $N \times N$ identity matrix, and $\bar{\mathbf{A}}$ and $\bar{\mathbf{B}}$ are $N \times N$ influence coefficient matrices. With ϕ known on all boundary nodes, Equation (32) is a linear system of N equations and can be readily solved for N unknowns of $\partial \phi / \partial n$, using classical methods such as LU decomposition and Gauss elimination.

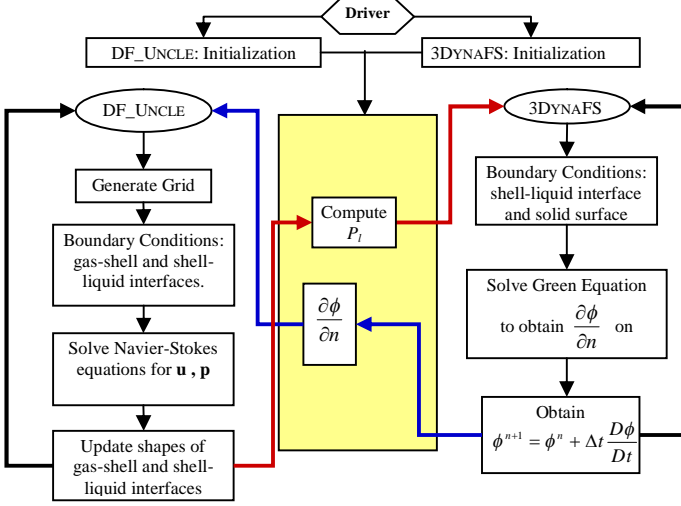


Figure 2. Flow chart of the numerical procedure for coupling the Navier-Stokes solver, DF_UNCLE[®], and the potential flow solver, 3DYNAFS[®].

2.4. Coupling between Inner and Outer Domain

The boundary conditions given by Equations (15), (19) and (26) are key for coupling the Navier-Stokes solver and the potential flow solver. The procedure is illustrated in Figure 2 and is summarized as follows:

- A volume grid is generated within each inner domain to discretize the shells according to the shape of the gas-shell interfaces and of the shell-liquid interfaces.
- The Navier-Stokes equations are solved for the velocity and pressure fields in the inner domains using the boundary conditions specified at the gas-shell interface with the gas pressure, p_g , and the shell-liquid interface with the normal velocity $\mathbf{u}_s \cdot \mathbf{n} = \partial \phi / \partial n$ provided by the potential solver. The gas-shell interface and the shell-liquid interface are updated according to the kinematic boundary condition and the boundary pressure P_i is calculated.
- The discretized Green's equation is solved for the normal velocity, $\partial \phi / \partial n$ on the boundary surfaces knowing the velocity potential ϕ . Using the boundary conditions specified at the shell-liquid interface with the boundary pressure P_i , provided by the Navier-Stokes solver, the rate of change of the potential $D\phi / Dt$ is obtained and the velocity potential ϕ at the next time step is updated.

2.5. Volume and Surface Grids

To solve the Navier-Stokes equations using the finite volume scheme, we discretize each *inner domain* describing the viscous thick shell using an O-type grid as shown in Figure 3. For most computations we select a grid number in the azimuthal direction of 41, 21 in the altitude, and 25 in the radial direction. The grid is evenly distributed in both azimuth and altitude directions while it is clustered near the air/shell and shell/liquid interface in the radial direction. Concerning the *outer domain* we use two types of grids Shown in Figure 4: an O-type structured grid and a triangular panel unstructured grid to represent the bubble outer surface. In the O-type structured grid, the grid points are the same as those in the outer surface of the grid used in DF_UNCLE[®] so that the exchange of variables between DF_UNCLE[®] and 3DYNAFS[®] is straightforward. However, since the singular points on the two poles result in low numerical precision in 3DYNAFS[®], we used the unstructured grid to solve the BEM problem. For the results shown below, we used a total number of 402 nodes and of 800 panels for the unstructured surface grids. Since the grid points are not the same as those used in the viscous code, the communication of the variables between DF_UNCLE[®] and 3DYNAFS[®] requires interpolation between the two grid systems and additional CPU time. However, using this unstructured grid is stable and avoids having singular unstable points as in the O-type grid.

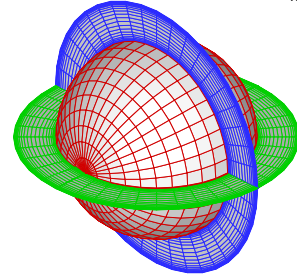


Figure 3. O-type grid used in DF_UNCLE[®] for the liquid shell (inner domain).

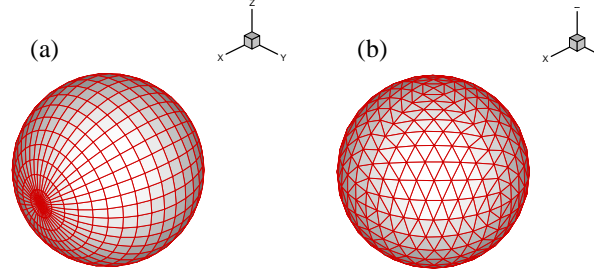


Figure 4. The two types of grids used in the outer domain for the 3DYNAFS[®] computations: (a) O-type structured grid, (b) Unstructured triangular-panels grid.

3. RESULTS AND DISCUSSION

3.1. Validation of Spherical Model

We have derived and implemented a 1D spherical thick shell model similar to that derived by Allen *et al.* [14] The derivation and resulting equations can be found in [25]. We

validated this model against experimental results found in [15], and then used it to validate the 3D shell model at different insonation conditions. Figure 5 shows a two-dimensional optical streak image of a triacetin-shelled bubble insonified by an acoustic pulse with a transmitted center frequency of 2.5MHz and peak negative pressure of 1.6MPa shown in the top of the figure from a hydrophone recording of the transmitted signal. The initial bubble radius was 1.7 μm . In Figure 5(a) our numerical solution (red curve) is laid over the optical image. A quantitative comparison of the time history of the radius of the contrast agent is shown in Figure 5(b). It can be seen that the 1-D spherical model reasonably captures the contrast agent oscillations amplitude and period except, as expected when the breakup occurs.

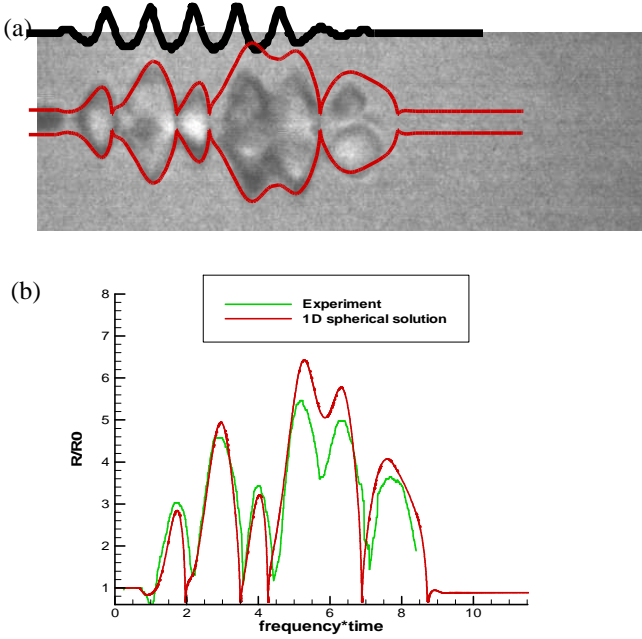


Figure 5. Comparison of the spherical thick shell model results with a streak image of a triacetin-shelled bubble with initial radius of 1.7 μm under insonation at 2.5MHz and 1.6MPa, (a) overlaid numerical solution and image of bubble outer shape, and hydrophone recording of transmitted pulse, (b) comparison of time history of contrast agent outer radius.

3.2. Validation of 3-D Model using Spherical Model

3.2.1. Small Amplitude Driving Pressure

To validate our 3-D numerical model, we first simulate the motion of a triacetin-shelled contrast agent driven by an acoustic pressure in an infinite medium. In this case, the bubble is expected to remain spherical during the oscillations and the results should be the same as those predicted using the 1-D spherical model. Figure 6 shows a comparison between the 3-D and spherical models. This is illustrated using the inner and outer radial motions of the contrast agent driven by a sinusoidal acoustic wave with $P_a = 0.1\text{Mpa}$ and $f = 3\text{MHz}$ at an ambient pressure of 0.1Mpa. The initial inner radius of the contrast agent is $R_{i0} = 1.2 \mu\text{m}$ and the outer radius is $R_{o0} = 1.7 \mu\text{m}$. The radii in the figure are normalized by R_{i0} and the time is normalized

by $R_{i0}\sqrt{\rho/P_a}$. The comparison shows that the 3-D numerical results agree very well with the spherical solution with very small differences resulting from the non perfect discretization of the sphere.

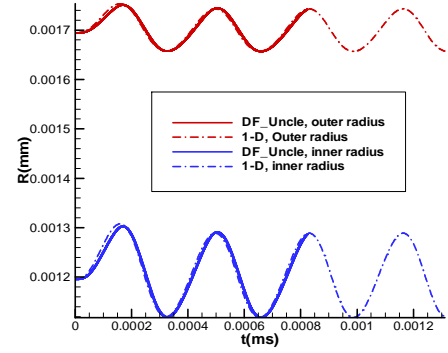


Figure 6. A triacetin-shelled bubble driven by a sinusoidal acoustic wave with $P_a=0.1\text{Mpa}$, $P_{atm}=0.1\text{Mpa}$ and $f=3\text{MHz}$. Comparison between 3D and spherical solutions.

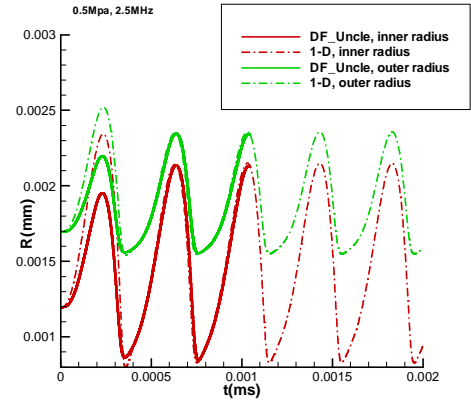


Figure 7. A triacetin-shelled bubble driven by a sinusoidal pressure with $P_a=0.5\text{Mpa}$, $P_{atm}=0.1\text{Mpa}$, and $f=2.5\text{MHz}$. Comparison between 3D and spherical solutions.

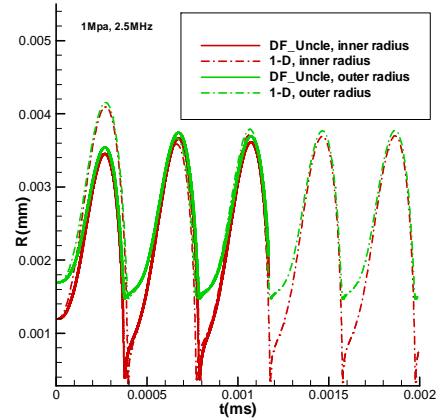


Figure 8. A triacetin-shelled bubble driven by $P_a=1\text{Mpa}$, $P_{atm}=0.1\text{Mpa}$, and $f=2.5\text{MHz}$. Comparison between 3D and spherical solutions.

3.2.2. Large Amplitude Driving Pressure

Figure 7 and Figure 8 show the radial motion of the contrast agent bubble driven at $f = 2.5\text{MHz}$ with $P_a = 0.5\text{MPa}$ and 1MPa respectively. Here the pressure amplitudes are much larger than in the previous case and bubble oscillations are more intense. During the first period, there are large differences between the 3-D results and the spherical model results. The 3-D code appears too sensible to transients and may require an improved time stepping scheme further at the start of the dynamics. However, the results become very close after the first bubble oscillation period.

Figure 9 and Figure 10 show a comparison of the minimum shell thickness between the 3-D and 1-D results at three different frequencies for the first and second bubble periods, respectively. The lines show the 1-D spherical model predictions while the symbols show the 3-D numerical simulations. The colors represent different frequencies. The relative differences of the numerical results of the first and second maxima with different pressure amplitudes are shown in Figure 11. With small amplitudes, the 3D numerical solutions agree with the 1-D spherical solution while for large amplitudes, the numerical solutions agree with the 1-D spherical solution only after the second bubble period.

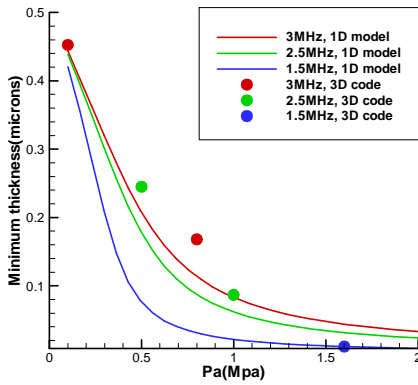


Figure 9. Comparison of the minimum shell thickness during the first bubble period.

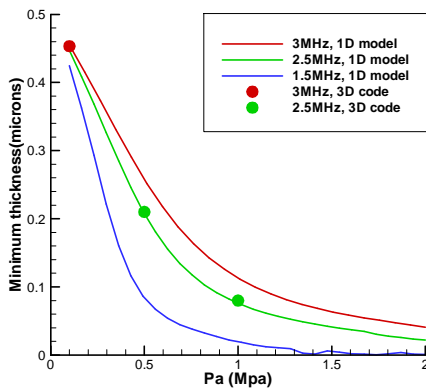


Figure 10. Comparison of the minimum shell thickness during the second bubble period.

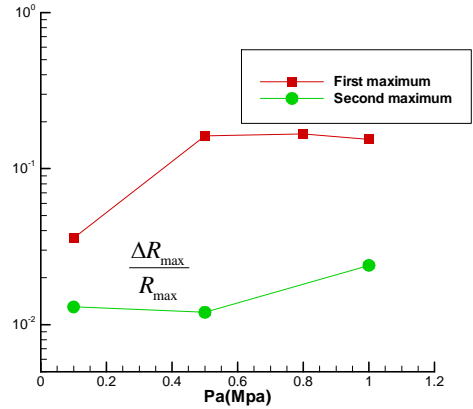


Figure 11. Relative difference between the 3D code simulations and the spherical solution.

3.3. Contrast Agent Dynamics near Rigid Wall

When a contrast agent bubble oscillates near a wall, its dynamics deviate from spherical oscillations. To simulate contrast agent dynamics near a wall, a rigid boundary is added in the outer computational domain. There are two ways of doing this: one way is to actually discretize the solid wall with a boundary element mesh in addition to the contrast agent as shown in Figure 12. The other way is to indirectly account for the wall by adding an image of the contrast agent relative to the wall, as shown in Figure 13. For the simulations presently below, we have used the image method.

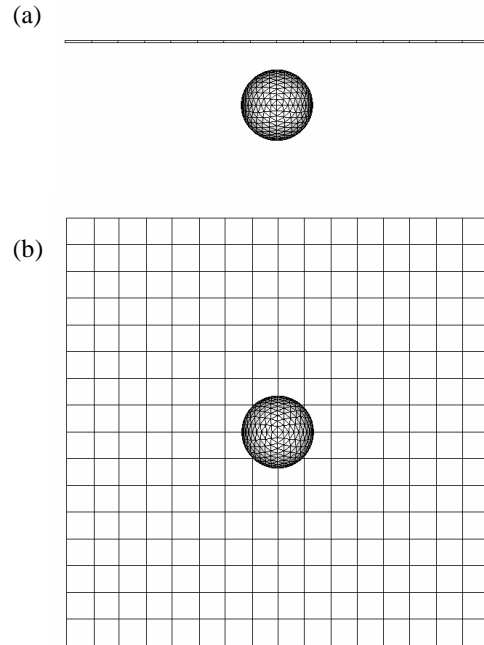


Figure 12. Geometrical setup of the contrast agent dynamics near a discretized wall (a) side view (b) top view.

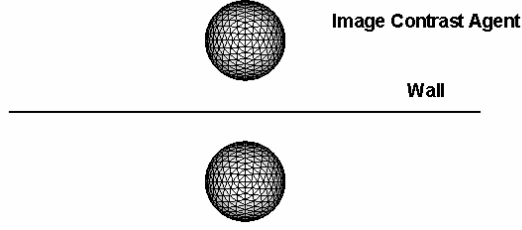


Figure 13. Geometrical setup of the contrast agent dynamics near a wall using an image bubble.

3.3.1. Small Amplitude Driving Pressure

With a small amplitude driving pressure, the non-spherical deformations are small, however, the motion of the volume center of the contrast agent (based on the shell/liquid interface) is not negligible. Figure 14 shows the x-coordinates of the shelled bubble center when the bubble is driven at $P_{am} = 0.1\text{Mpa}$, $P_a = 0.1\text{Mpa}$, and $f = 3\text{MHz}$ in presence or absence of a rigid wall. The contrast agent initial inner and outer radii are $R_{10} = 1.2\ \mu\text{m}$ and $R_{20} = 1.7\ \mu\text{m}$ respectively. The contrast agent is initially located at $X = 0$ and the wall is located at $X = 1.715\ \mu\text{m}$. The figure shows that the shelled-bubble center moves away from wall during expansion then gets closer to the wall during compression. For the spherical bubble the center of the contrast agent obviously does not move.

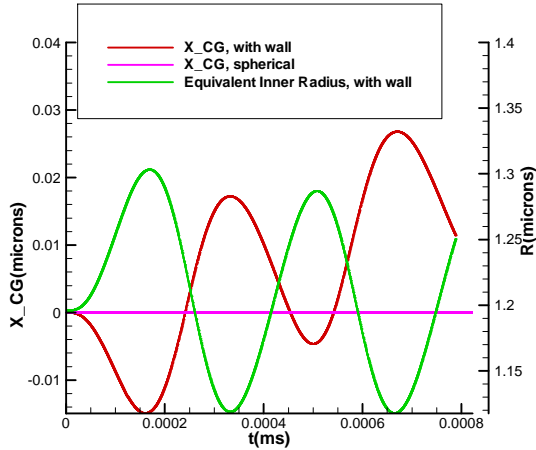


Figure 14. The location of the center of gravity of the contrast agent driven near a wall by a sinusoidal acoustic wave with $P_a = P_{am} = 0.1\text{Mpa}$ and $f = 3\text{MHz}$.

3.3.2. Large Amplitude Driving Pressure

The non-spherical deformations due to the presence of the wall become much more significant and interesting as the driving pressure amplitude becomes higher. It is known from previous studies [5-7] that non-spherical dynamics can result in the formation of re-entrant jets directed towards rigid walls or moving away from free surfaces [23]. To study the effect of a rigid wall on contrast agent dynamics, we present below 3-D numerical simulations for an acoustically excited contrast agent oscillating near a rigid wall at three different initial standoffs,

$X = 2.6, 3.6$ and $4.6\ \mu\text{m}$. The contrast agent initial inner radius is $R_{10} = 1.2\ \mu\text{m}$ and its outer radius is $R_{20} = 1.7\ \mu\text{m}$.

Figure 15 through Figure 17 show for the three standoffs the contrast agent shape time variations during the first oscillation period. Also shown are the pressure contours in the viscous liquid of the shell. All shapes are shown in a cut plane perpendicular to the wall and going through the bubble center. The shelled bubble was initially in a uniform pressure field with $P_{am} = 0.1\text{Mpa}$, and was subjected to a sinusoidal acoustic wave with $P_a = 1\text{Mpa}$ and $f = 2.5\text{MHz}$. As expected, the smallest standoff case has the most significant non-spherical deformations. The presence of the wall imparts a non-spherical pressure distribution on the shell which deforms it non-spherically. More importantly the dynamics lead to a non-uniform shell liquid thickness distribution during the collapse. During the bubble growth phase, the shell retains a more or less uniform thickness, then becomes thicker and thicker on the side opposed to the wall, where a jet usually takes place. Concurrently, the shell becomes thinner and thinner at the side nearest to the wall potentially leading to starvation of the shell liquid and potential breakup. Using a linear stability analysis [25], we have also confirmed that the most unstable mode due to a 3-D perturbation is when the bubble form a jet at one end and breaks up on the other end.

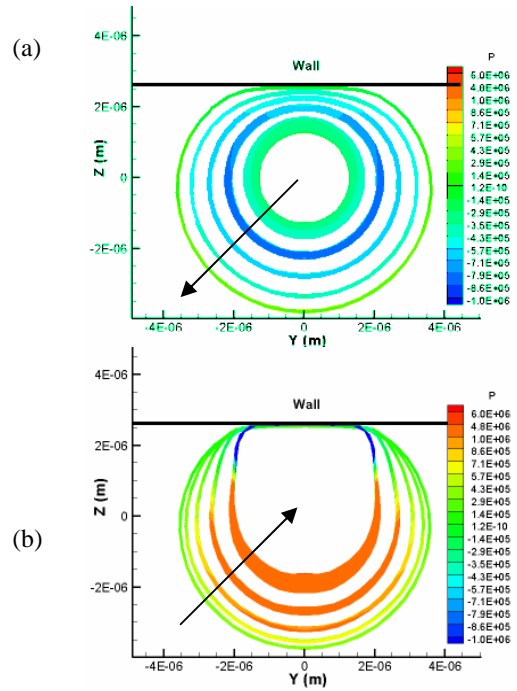


Figure 15. Contrast agent shape variations and pressure contours near a rigid wall when subjected to a sinusoidal acoustic wave with $P_a = 1\text{Mpa}$, $P_{am} = 0.1\text{Mpa}$ and $f = 2.5\text{MHz}$. Initial standoff of $2.6\ \mu\text{m}$. (a) bubble growth and (b) bubble collapse with $R_{10} = 1.2\ \mu\text{m}$, $R_{20} = 1.7\ \mu\text{m}$.

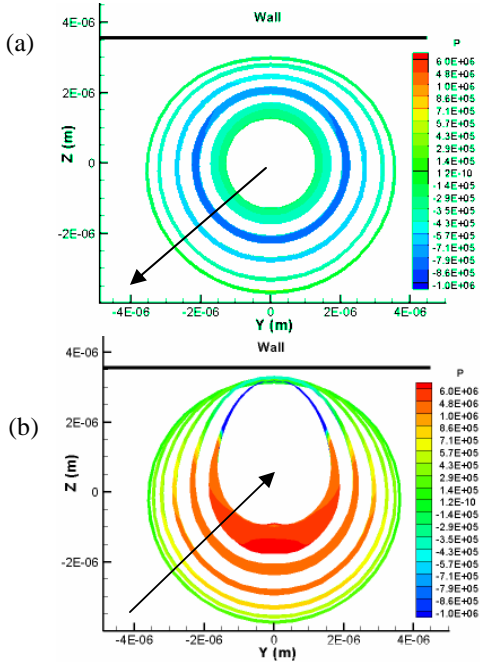


Figure 16. Contrast agent shape variations and pressure contours near a rigid wall when subjected to a sinusoidal acoustic wave with $P_a = 1\text{Mpa}$, $P_{atm} = 0.1\text{Mpa}$ and $f = 2.5\text{MHz}$. Initial standoff of $3.6\ \mu\text{m}$. (a) bubble growth and (b) bubble collapse with $R_{10} = 1.2\ \mu\text{m}$, $R_{20} = 1.7\ \mu\text{m}$.

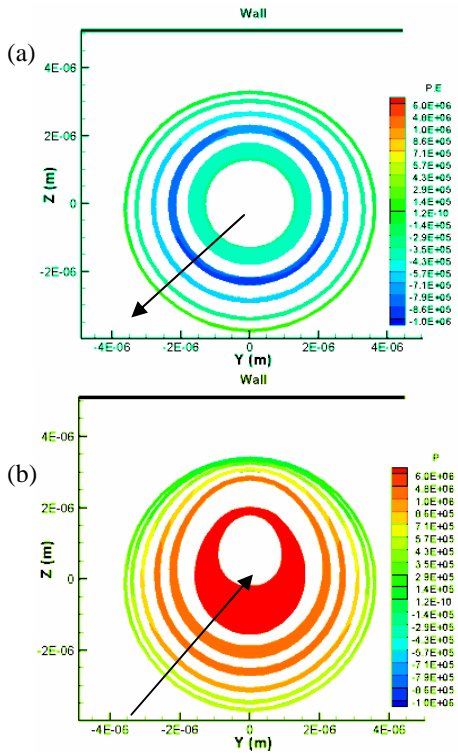


Figure 17. Contrast agent shape variations and pressure contours near a rigid wall as seen in the inner domain when subjected to a sinusoidal acoustic wave with $P_a = 1\text{Mpa}$, $P_{atm} = 0.1\text{Mpa}$ and $f = 2.5\text{MHz}$. Initial standoff of $4.6\ \mu\text{m}$. (a) bubble growth and (b) bubble collapse with $R_{10} = 1.2\ \mu\text{m}$, $R_{20} = 1.7\ \mu\text{m}$.

Figure 18 through Figure 20 show the contrast agent shape variations and normal velocity contours at three time steps as seen in the outer domain in which two contrast agents are present due to the plane of symmetry used. In the figures, the second set is at the time the contrast agent grew to its maximum size while the third set is the last time step before the simulations were terminated for the $X = 2.6$ and $3.6\ \mu\text{m}$ cases. This is the last time step before the rebound for the $X = 4.6\ \mu\text{m}$ case.

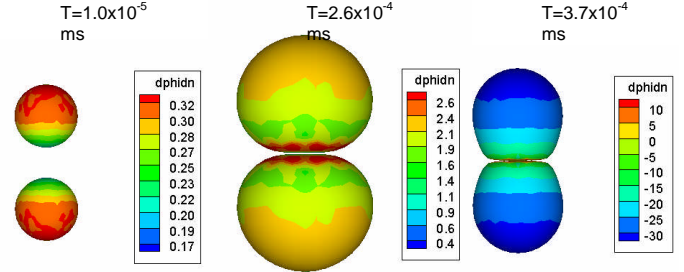


Figure 18. Contrast agent shape variations and normal velocity 3D contours at three times as seen in the outer domain. Excitation sinusoidal acoustic wave with $P_a = 1\text{Mpa}$, $P_{atm} = 0.1\text{Mpa}$ and $f = 2.5\text{MHz}$ at an initial standoff of $2.6\ \mu\text{m}$ with $R_{10} = 1.2\ \mu\text{m}$, $R_{20} = 1.7\ \mu\text{m}$.

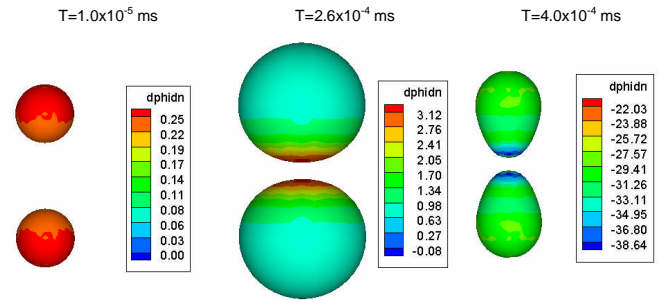


Figure 19. Contrast agent shape variations and normal velocity contours at three time steps as seen in the outer domain. Excitation by a sinusoidal acoustic wave with $P_a = 1\text{Mpa}$, $P_{atm} = 0.1\text{Mpa}$ and $f = 2.5\text{MHz}$ at an initial standoff of $3.6\ \mu\text{m}$ with $R_{10} = 1.2\ \mu\text{m}$, $R_{20} = 1.7\ \mu\text{m}$.

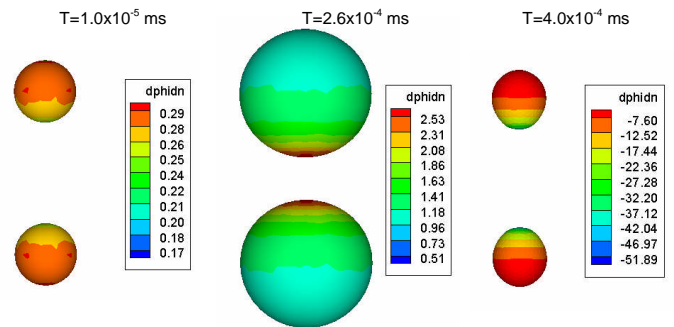


Figure 20. Contrast agent shape variations and normal velocity contours at three time steps as seen in the outer domain. Excitation by a sinusoidal acoustic wave with $P_a = 1\text{Mpa}$, $P_{atm} = 0.1\text{Mpa}$ and $f = 2.5\text{MHz}$ at an initial standoff of $4.6\ \mu\text{m}$ with $R_{10} = 1.2\ \mu\text{m}$, $R_{20} = 1.7\ \mu\text{m}$.

Figure 21 shows a comparison of the time history of the contrast agent equivalent radius for the three standoff cases. It is seen that the presence of the wall only has a slight influence on the maximum growth size of the contrast agent.

The simulations for the $X = 2.6$ and $3.6 \mu\text{m}$ cases, however, were terminated due to numerical instability as the shell became extremely thin and the 3D grid became overly squeezed, while the simulation for the $X = 4.6 \mu\text{m}$ case was able to continue and the rebound was observed.

Figure 22 shows the solutions with the velocity vectors plotted on both shell/liquid and shell/gas interfaces at the last time step before the simulations were terminated for the $X = 2.6$ and $X = 3.6 \mu\text{m}$ cases. Figure 23 shows the solutions at the time steps before and after the rebound for the $X = 4.6 \mu\text{m}$ cases. It is seen that, at the time the computations stopped for the $X = 2.6$ and $3.6 \mu\text{m}$ cases, a re-entrant jet with a high normal velocity was just starting to form at the thick-shell side while the shell was stretching with a high tangential velocity component at the thin-shell side. Continuous shell thinning and stretching at the near-wall side indicate the tendency of the shell to break up. For the $X=4.6 \mu\text{m}$ case, the shell remained thick everywhere and was not stretched near the wall side. As a result the contrast agent was able to rebound after reaching its minimum volume.

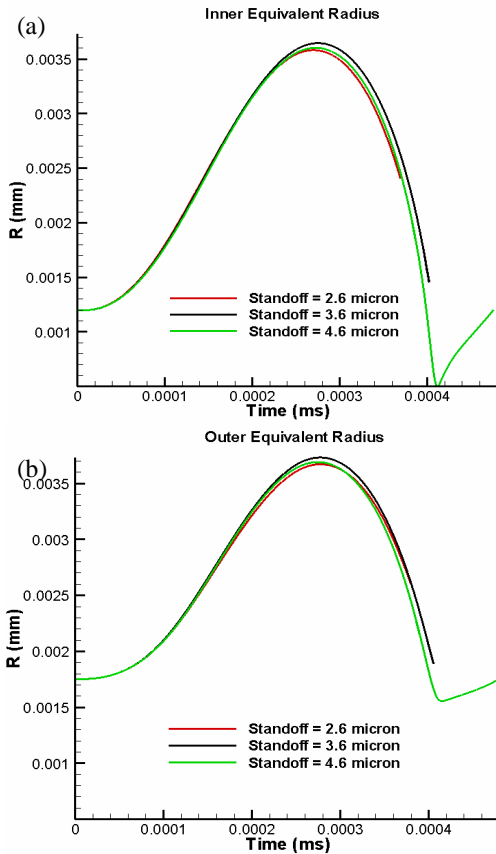


Figure 21. Contrast agent equivalent radius versus time for three different standoff cases; (a) inner equivalent radius vs. time, and (b) outer equivalent radius vs. time.

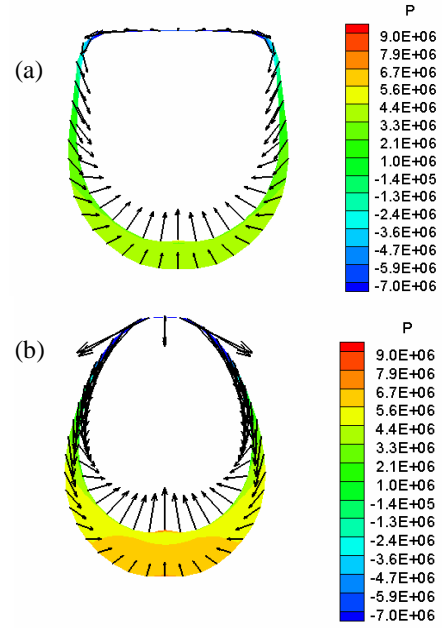


Figure 22. Contrast agent shape near a wall at the last time step before the simulations were terminated for (a) $X = 2.6$, and (b) $3.6 \mu\text{m}$ cases. The velocity vectors are shown plotted on both the shell/liquid and the shell/gas interface.

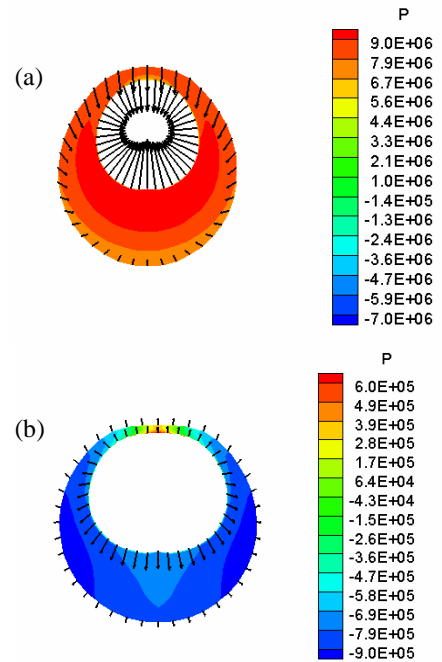


Figure 23. Contrast agent shape near a wall at the time steps before and after rebound for the $X = 4.6 \mu\text{m}$ case. The velocity vectors are shown plotted on both the shell/liquid and the shell/gas interfaces.

3.4. Contrast Agent Dynamics between Two Walls

To demonstrate the capabilities of the developed 3-D model, we have simulated the dynamics of two contrast agent bubbles located between two discretized walls separated by a

distance of 12 μm (Figure 24). The shelled bubbles were subjected to a sinusoidal acoustic wave with $P_{atm} = 0.1\text{Mpa}$, $P_a = 1\text{Mpa}$ and $f = 2.5\text{MHz}$. Figure 25 shows the contrast agent shape variations and pressure contours during the first oscillation period. It is seen that the presence of the two walls leads the contrast agent bubbles to oscillate in oval shapes with the axes switching between horizontal and vertical directions during growth and collapse. Figure 26 shows the contrast agent shape variations and normal velocity contours at two time steps.

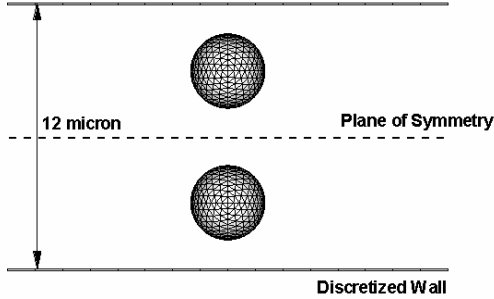


Figure 24. Numerical setup of the outer computational domain for two contrast agent bubbles between two walls.

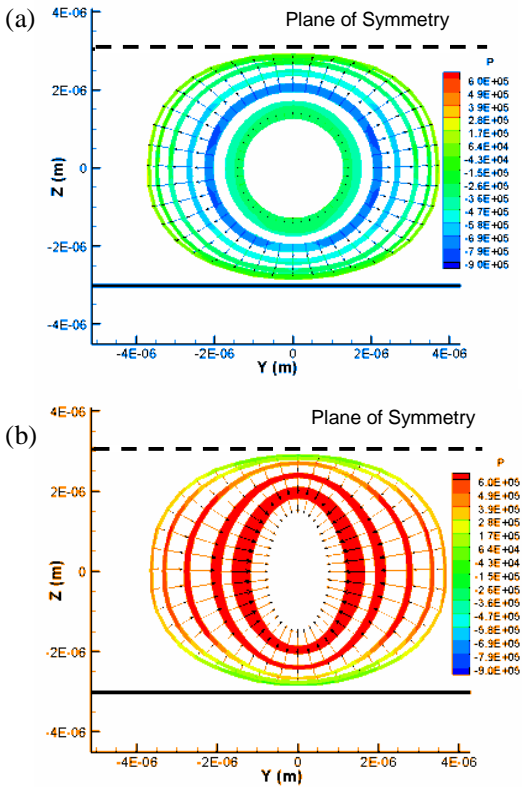


Figure 25. Contrast agent shape variations and pressure contours for two contrast agents in between two walls subjected to a sinusoidal acoustic wave with $P_a = 1\text{Mpa}$, $P_{atm} = 0.1\text{Mpa}$ and $f = 2.5\text{MHz}$ during (a) growth and (b) collapse during the first oscillation period.

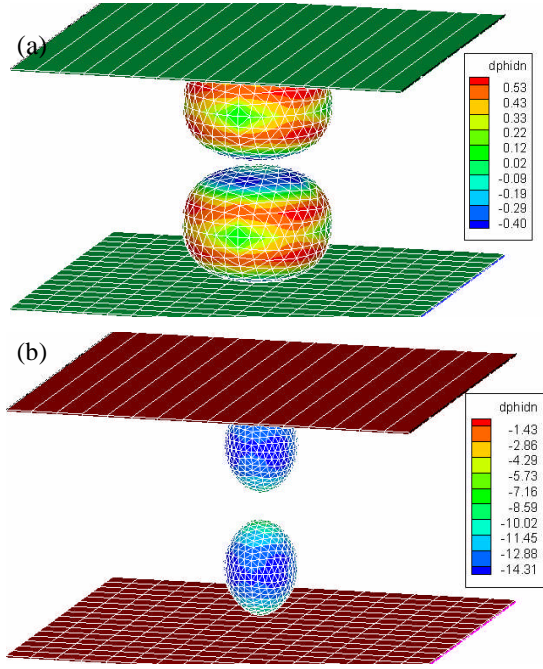


Figure 26. Contrast agent shape variations and normal velocity contours for two contrast agent bubbles in between two walls at two time steps. Excitation by a sinusoidal acoustic wave with $P_a = 1\text{Mpa}$, $P_{atm} = 0.1\text{Mpa}$ and $f = 2.5\text{MHz}$.

4. CONCLUSIONS

In this study we have considered the dynamics of thick viscous shell contrast agents. We have developed a 3-D thick viscous shell model where the dynamics of the shell material was followed using a Navier Stokes solver, while the dynamics of the overall bubble was described with a boundary element method. This shell model allowed us to simulate multiple contrast agent dynamics and their interactions with nearby solid walls. We have validated this model with experimental results available in the literature for spherical deformations. Further validation is needed for non-spherical deformations.

We also exercised this model under different conditions and have derived the following conclusions:

- The thick viscous shell prevents the contrast agent from forming a re-entrant jet towards a nearby boundary.
- The shell thickness varies significantly from location to location during the thick shell dynamics.
- The thick shelled contrast agent may break up due to local shell thinning and stretching.

Our simulations seem to indicate that in the presence of a wall of another interaction contrast agent, the shell thinning and thus potential for breakup occurs on the shell side nearest to the wall or to the other agent.

ACKNOWLEDGMENTS

This work was supported by the National Institute of Biomedical Imaging and Bioengineering, NIH under an SBIR Phase I program.

REFERENCES

- 1 Raisinghani, A. & Demaria, A.N., "Physical principles of microbubble ultrasound contrast agents," *The American Journal of Cardiology*, **90**, 10A, 3J-7J, 2002
- 2 Unger, E., McCreery, T.P., Sweitzer, R., Caldwell, V. & Wu, Y., "Acoustically active lipospheres containing paclitaxel: A new therapeutic ultrasound contrast agent," *Invest Radio*, **12**, 886-892, 1998.
- 3 Chang, P.P., Chen, W.S., Mourad, P.D., Poliachik, S.L. & Crum, L.A., "Thresholds for inertial cavitation in Alunex suspensions under pulsed ultrasound conditions," *IEEE Trans Ultrason. Freq. Control*, **48**, 161-170, 2001.
- 4 Chen, W.S., Matula, T. J., Brayman, A.A. & Crum, A.A., "A Comparison of the fragmentation thresholds and inertial cavitation doses of different ultrasound contrast agents," *J. Acoust. Soc. Am.* **113** (1), 643-651, 2003.
- 5 Chahine, G.L., "Experimental and asymptotic study of nonspherical bubble collapse," *Applied Scientific Research*, **38**, 187-197, 1982.
- 6 Chahine, G.L., "Cavitation dynamics at microscale level," *Journal of Heart Valve Disease*, **3**, 102-116, 1993
- 7 Zhang, S., Duncan, J. H., & Chahine, G.L., "The final stage of the collapse of a cavitation bubble near a rigid wall," *J. Fluid Mech.*, **257**, 147-181, 1993.
- 8 Miller, M. W., "Gene transfection and drug delivery," *Ultrasound in Med. & Biol.* **26**, S59-S62, 2000.
- 9 Church, C.C., "The effects of an elastic solid surface layer on the radial pulsations of gas bubbles," *J. Acoust. Soc. Am.*, **97**(3), 1510-1521, 1995.
- 10 Allen, J.S., Kaneko, Y., Yoshizawa, S. & Matsumoto, Y., "Development and application of contrast agent model," *Fifth International Symposium on Cavitation*, Osaka, Japan, November 1-4, 2003.
- 11 Hoff, L., Sontum, P.C. & Hovem, J.M., "Oscillations of polymeric microbubbles: Effect of the encapsulating shell," *J. Acoust. Soc. Am.*, **107**(4), 2272-2280, 2000.
- 12 Ma, J., Yu, J., Fan, Z., Zhu, Z., Gong, X. & Du, G., "Acoustic nonlinearity of liquid containing encapsulated microbubbles," *J. Acoust. Soc. Am.*, **116**(1), 186-193, 2004.
- 13 Sarkar, K, Shi, W.T., Chatterjee, D. & Forsberg, F., "Characterization of ultrasound contrast microbubbles using in vitro experiments and viscous and viscoelastic interface models for encapsulation," *J. Acoust. Soc. Am.*, **119**(1), 2005.
- 14 Allen, J.S., May, D.J. & Ferrara, K.W., "Dynamics of therapeutic ultrasound contrast agents," *Ultrasound in Med. & Biol.*, **29**(6), 805-816, 2002.
- 15 May, D. J., Allen, J.J. & Ferrara, K.W., "Dynamics and fragmentation of thick-shelled microbubbles," *IEEE Transactions on Ultrasonics, Ferroelectrics, and Frequency Control*, **49**(10), 1400-1410, 2002.
- 16 Batchelor, G. K., *Fluid Dynamics*, Cambridge University Press., 1967.
- 17 Hodges, B., Street, R. & Zang, Y. A method for simulation of viscous nonlinear free-surface flows. *20th Symposium on Naval Hydrodynamics*, 791-809, 1996.
- 18 Chorin, A. J., "A numerical method for solving incompressible viscous flow problems," *Journal of Computational Physics*, **2**, 12-26, 1967.
- 19 Roe, P. L., "Approximate Riemann solvers parameter vectors and difference schemes," *Journal of Computational Physics*, **43**, 357-372, 1981.
- 20 van Leer, B., "Towards the ultimate conservative difference scheme. Second order sequel to Godunov's method," *Journal of Computational Physics*, **32**, 101-136, 1979.
- 21 Vanden, K. & Whitfield, D. L., "Direct and iterative algorithms for the three-dimensional Euler equations," AIAA-93-3378, 1993 .
- 22 Chahine, G. L. & Duraiswami, R., "Method for calculating 2-D and 3-D underwater explosion bubble behavior in free water and near structures," NSWC Dahlgren Division Report NSWCDD/TR-93/44 (limited distribution), 1993.
- 23 Chahine, G.L., "Interaction between an oscillating bubble and a free surface," *Journal of Fluids Engineering*, **99**, 709-716, 1977.
- 24 Chahine, G.L., Perdue, T.O. & Tucker, C.B., "Interaction between underwater explosion bubble and a solid submerged body," DYNFLOW INC. Technical Report 89001-1, August. 1989.
- 25 Hsiao, C.T., Lu, X.Z., and Chahine, G.L., "3D Modelling of the dynamics of therapeutic ultrasound contrast agents," DYNFLOW, INC. Report 2M6018-NIH-1, May 2007.